Current-perpendicular-to-plane magnetoresistance of ferromagnetic F/Al interfaces ($F=$Py, Co, Fe, and $\mathrm{Co_{91}Fe_9}$) and structural studies of Co/Al and Py/Al

A. Sharma, N. Theodoropoulou, T. Haillard, R. Acharyya, R. Loloee, W. P. Pratt, Jr., and J. Bass
Physics Department, Michigan State University, East Lansing, Michigan 48824, USA

J. Zhang and M. A. Crimp
Department of Chemical Engineering and Materials Science, Michigan State University, East Lansing, Michigan, 48824, USA

(Received 20 November 2007; revised manuscript received 16 April 2008; published 26 June 2008)

We determined current-perpendicular-to-plane magnetotransport parameters: interface specific resistance ($2AR^*$) and scattering asymmetry (γ) for F/Al (F: Py=$\mathrm{Ni_{84}Fe_{16}}$, Co, Fe, and $\mathrm{Co_{91}Fe_9}$) interfaces. The derived values of $2AR^* \sim 8.4-11.6$ fΩ m^2 are exceptionally large but those of $\gamma < 0.18$ are small. Modest changes in sample resistances with aging and annealing indicated some changes in interfacial structure. We studied those changes in Co/Al and Py/Al multilayers, using high resolution transmission electron microscopy and electron energy loss spectroscopy. These techniques showed little, if any, differences in interfacial structure and width between unannealed and annealed multilayers and no evidence of intermetallic phase formation. The structural differences that cause the transport differences, thus, appear to be subtle.

DOI: 10.1103/PhysRevB.77.224438 PACS number(s): 75.70.Cn, 73.40.−c

I. INTRODUCTION

The performance of potential current-perpendicular-to-plane (CPP) magnetoresistance (CPP-MR) based read-heads and current-induced-magnetization-switching based magnetic random access memory, based upon a combination of ferromagnetic (F) and nonmagnetic (N) metals, could be enhanced by discovery of F/N pairs with large values of both of the interface parameters: the enhanced specific resistance, $2AR^*_{F/N}$ (R=sample resistance and A=area though which the CPP-current flows), and the scattering asymmetry $\gamma_{F/N}$, each of which will be defined below. Standard F/N pairs such as Co/Cu and Py/Cu (Py=$\mathrm{Ni_{1-x}Fe_x}$ with $x \sim 0.2$) have large $\gamma_{F/N} \sim 0.7-0.8$ but modest $2AR^*_{F/N} \sim 1$ fΩ m^2.[1] Stimulated by evidence from Garcia *et al.*[2] that the interface of Py/Al might have drastically different spin-dependent scattering properties from that of Py/Cu, we first determined the interface parameters for Py/Al using our well-established CPP-MR technique.[3] We found unusually large $2AR^*_{\mathrm{Py/Al}} \sim 8.6$ fΩ m^2, but small $\gamma_{\mathrm{Py/Al}} \sim 0.03$. This result led us to extend measurements to other F/Al pairs (F=Co, $\mathrm{Co_{0.91}Fe_{0.9}}$, and Fe) in hopes of finding a large $2AR^*_{F/N}$ combined with larger $\gamma_{F/N}$. Although we again found large $2AR^*_{F/\mathrm{Al}} \sim 9-10$ fΩ m^2, we also again found small $\gamma_{F/\mathrm{Al}} \leq 0.1$.[4] Moreover, we found that the resistances of all of the F/Al samples were somewhat unstable over time and with annealing to a temperature $\sim$450 K, changes not completely unexpected as we explain below.

In this paper, we: (a) present complete resistance results for these four different F/Al sample pairs, including explicit changes with time and with annealing to 450 K; (b) explain why we expect the interdiffusion that causes the observed changes in resistance with time and annealing temperature, and (c) present transmission electron microscopy (TEM), high resolution transmission electron microscopy (HRTEM), and electron energy loss spectroscopy (EELS) studies of the structural differences between as-sputtered and annealed samples (which turn out to be mostly modest). New data that we recently obtained on our Fe, included as an Appendix, leads to a change in the values of $2AR^*_{\mathrm{Fe/Al}}$ and $\gamma_{\mathrm{Fe/Al}}$ from those given in Ref. 4. We also consider an alternative analysis of Co/Al, necessitated by an inconsistency uncovered by the initial analysis.

The paper is organized as follows: In Sec. II, we define the parameters of interest, describe our samples, and give details of how they are prepared and measured. In Sec. III, we describe the equations we use for analysis and apply them to derive the parameters $2AR^*_{F/\mathrm{Al}}$ and $\gamma_{F/\mathrm{Al}}$ from magnetotransport data for the as-prepared samples. To show effects of aging and annealing, we present results of measurements repeated after several months and/or after annealing to 450 K. In Sec. IV we explain what we hoped to learn from TEM-based studies, and then describe our TEM, HRTEM, and EELS techniques and the results obtained. In Sec. V, we summarize and conclude. The Appendix contains magnetoresistance data for exchange-biased spin-valves (EBSVs) of the form FeMn/Fe/Cu/Fe, which we use to determine the bulk asymmetry parameter β_{Fe} and the spin-diffusion length ℓ^{Fe}_{sf} for the Fe used in the present study and a prior one.[4]

II. PARAMETERS AND SAMPLES

A. Parameters

The physics of spin-polarized transport involves asymmetric scattering, both within F-layers and at F/N interfaces, of electrons with moment along ($\uparrow$) or opposite to ($\downarrow$) the direction of the local magnetization, $\boldsymbol{M}$. In this paper we focus upon the interface parameters, which in the CPP geometry can be characterized by two equivalent pairs.[5,6] The first pair, $AR^{\uparrow}_{F/N}$ and $AR^{\downarrow}_{F/N}$, are the specific resistances that measure the ability of electrons with moments along ($\uparrow$) or opposite to ($\downarrow$) the direction of magnetization of the F-metal to propagate from the N to F-metal or vice versa. The second pair, more convenient for analyzing experimental data, are twice the enhanced interface specific resistance, $2AR^*_{F/N}$

$=(AR^{\uparrow}_{F/N}+AR^{\downarrow}_{F/N}/2)$, and the dimensionless interface scattering asymmetry, $\gamma_{F/N}=(AR^{\downarrow}_{F/N}-AR^{\uparrow}_{F/N})/(AR^{\uparrow}_{F/N}+AR^{\downarrow}_{F/N})$. Large values of both $2AR^{*}_{F/N}$ and $\gamma_{F/N}$ imply that electron propagation from N to F is difficult for one moment direction, but easy for the other. In the CPP geometry, the equivalent bulk parameters within the F-metal are characterized by $\rho^{\uparrow}_{F}$ and $\rho^{\downarrow}_{F}$ or, the better pair for analysis, the enhanced resistivity, $\rho^{*}_{F}=(\rho^{\uparrow}_{F}+\rho^{\downarrow}_{F})/4=\rho_F/(1-\beta^{2}_{F})$, and the bulk scattering asymmetry, $\beta_F=(\rho^{\downarrow}_{F}-\rho^{\uparrow}_{F})/(\rho^{\downarrow}_{F}+\rho^{\uparrow}_{F})$, where ρ_F is the separately measurable resistivity of the F-metal in zero magnetic field. The values of ρ_F are directly measured as described in Sec III. The values of β_F are taken as known from other studies (except for Fe, see Appendix), and are listed with their sources in Sec III. $2AR^{*}_{F/N}$ and $\gamma_{F/N}$ are the only two unknowns to be determined from our experiments.

If the spin-diffusion (spin-flipping) lengths in the F and Al metals, l^{F}_{sf} and $l^{\mathrm{Al}}_{\mathrm{sf}}$, are longer than the F and Al layer thicknesses, t_F and t_{Al}, CPP-MR data can be analyzed in terms of a simple two current series resistor (2CSR) model that involves only the parameters just defined and the layer thicknesses t_F and t_{Al}. If either l^{F}_{sf} or $l^{\mathrm{Al}}_{\mathrm{sf}}$, or both, are smaller than t_F and t_{Al}, data analysis requires the more complicated Valet–Fert (VF) equations, which take the spin-diffusion lengths into account. As described in Sec. III, we use the 2CSR model for our $[F/N]_n$ multilayers, where t_F is kept fixed at $t_F=6$ nm but the VF model for our exchange-biased spin-valves (EBSVs), where $t_F=24$ nm. The values of l^{F}_{sf} for the VF model are taken from prior studies (except for $l^{\mathrm{Fe}}_{\mathrm{sf}}$, see Appendix) and are listed in Sec. III with references. In the present paper, we neglect any potential spin-flipping at the F/N interfaces,[7] except for one case, where we seem to need it for complete internal consistency.

B. Samples

To obtain a uniform CPP-current in short-wide samples, our samples were deposited in our standard crossed-superconducting-Nb-strips geometry, using a sputtering system and the procedures previously described.[8,9] Crossed Nb strips, 150-nm thick and ~1.1-mm wide, sandwich the multilayer of interest. At the measuring temperature of 4.2 K, the Nb strips stay superconducting in the modest magnetic fields used for the measurements. The samples were sputtered at substrate temperatures between 243 and 295 K, in an ultrahigh vacuum compatible system, with an *in situ* process for changing masks without breaking vacuum, and precleaned argon sputtering gas. The area A ~1.2 mm^2 through which the CPP-current flowed was determined as the product of the measured widths of the two Nb cross strips. The sample resistances, typically 10^{-9} to 10^{-8} Ω, were measured with a measuring current of 0.1 A and a superconducting quantum interference device based bridge circuit having a sensitivity and noise limit better than 10^{-11} Ω.[8]

In the present study, we measured the resistances of two kinds of samples. The first kind are multilayers of the form $\{[F(6)/\mathrm{Al}(t_{\mathrm{Al}})]_n/F(6)\}$ with fixed $t_F=6$ nm chosen so that l^{F}_{sf} is comparable to or larger than t_F. Here n is the number of bilayer repeats, the thicknesses are in nanometers and the sample has total thickness $t_T=n(6+t_{\mathrm{Al}})+6=366$ nm. The two outer layers of the multilayers are F to eliminate any proximity effect on the Al layers from the superconducting Nb cross strips. Since, as we will see below, we expect $l^{\mathrm{Al}}_{\mathrm{sf}}$ to be larger than any value of t_{Al} in such multilayers, we expect the 2CSR model to give a good approximation to the multilayer data.

The second kind is EBSVs consisting of only four layers; $[\mathrm{FeMn}(8)/F(24)/\mathrm{Al}(t_{\mathrm{Al}})/F(24)]$ between the Nb cross strips. Here, the magnetization of one F-layer is pinned by the adjacent FeMn antiferromagnet (AF) (Ref. 10), by heating the sample to 453 K, above the usual blocking temperature of polycrystalline FeMn (Ref. 11), applying a small magnetic field (~200 Oe) for ~2 min, and then cooling it quickly in the presence of the field. For our EBSVs, we choose $t_{\mathrm{Al}}>6$ nm, large enough so that the exchange coupling between the F-layers should be negligible, letting the other F-layer switch in small H. We also choose $t_F=24$ nm $\gg l^{F}_{\mathrm{sf}}$ (except for Co) to simplify the data analysis as we describe below.

In principle, if we could achieve true parallel (P) and antiparallel (AP) orderings of the magnetic moments of the F-layers in the multilayers, or reproduce sufficiently well the large background specific resistance of the EBSVs, either of the two sets of samples alone could be used to derive both $2AR^{*}_{F/N}$ and $\gamma_{F/N}$. However, inability to produce unequivocal AP states in the multilayers, and sample to sample variations in the total ARs of the EBSVs, led us to use the multilayers to first estimate $2AR^{*}_{F/N}$ and then the EBSVs to estimate $\gamma_{F/N}$. With these parameters in hand, we can predict the values of $A\Delta R$ for the multilayers and compare our predictions with the experimental data. In two of our four cases, CoFe/Al and Fe/Al, the predicted and experimental multilayer values of $A\Delta R$ are close enough that our values of $2AR^{*}_{F/\mathrm{Al}}$ and $\gamma_{F/N}$ are internally consistent. In one case, Py/Al, our predicted $A\Delta R$ is larger than the experimental one. Since similar behavior was seen previously in Py/Cu (see below), we conclude that Py simply does not give good AP states and there is no inconsistency in our values. In the last case, Co/Al, our predicted $A\Delta R$ is smaller than the experimental one. This difference is an inconsistency, which we discuss further below.

For HRTEM and EELS studies, separate multilayer films ($[F/N]_{10}$, with 10 Co (or Py)/Al bilayers were sputtered in the same chamber and under similar conditions to the samples on which we measured resistances. Each bilayer consisted of a 20 nm Co (or Py) layer and a 10 nm Al layer. To look for effects of annealing, some samples were annealed at 453 K for less than 5 min before being prepared for TEM.

III. RESISTANCE DATA, PARAMETERS, AND ANALYSIS

We estimated the resistivity of our Al, Py, Co, $\mathrm{Co_{91}Fe_9}$, and Fe by separately sputtering 200-nm thick films and measuring their in-plane resistivities by the van der Pauw technique.[12] The resulting low resistivity for Al, ρ_{Al} ~5 nΩ m, gives an expected very long spin-diffusion length $l^{\mathrm{Al}}_{\mathrm{sf}}\geq 500$ nm.[7] Independently measured spin-diffusion lengths of the ferromagnets used in this study are:

$l_{sf}^{Py}=5.5\pm1$ nm (Refs. 7 and 13); $l_{sf}^{Fe}=5\pm1$ nm (see Appendix); $l_{sf}^{Co}>40$ nm (Refs. 7 and 14) and $l_{sf}^{CoFe}=12\pm1$ nm (Refs. 7 and 15). With this large l_{sf}^{Al} and values of l_{sf} all comparable to or larger than the fixed F-layer thickness $t_F=6$ nm used in our multilayers, we should be able to analyze our multilayer data with a simple 2CSR model, provided that we can at least closely achieve the magnetically ordered state in which the moments of neighboring F-layers are ordered AP to each other.

Neglecting the difference between n and $n+1$, the form for AR^{AP} given by the 2CSR model is[1]

$$AR^{AP}=2AR_{S/F}+\rho_{Al}t_T+\rho_F^*t_F+n[t_F(\rho_F^*-\rho_{Al})+2AR_{F/Al}^*]. \quad (1)$$

The corresponding expression for $A\Delta R=AR^{AP}-AR^{P}$ is

$$A\Delta R=n^2(\beta_F\rho_F^*t_F+2\gamma_{F/Al}AR_{F/Al}^*)^2/AR^{AP}. \quad (2)$$

In Eq. (1), $2AR_{S/F}$ is the contribution from the interfaces between the outer F-layers and the superconducting Nb leads. For all the four ferromagnetic metals under study: Py, Co, Fe, and CoFe, $2AR_{S/F}^*=(6\pm1)$ fΩ m^2.[8–16] ρ_F^* is the enhanced resistivity defined above, and ρ_F and ρ_N are estimated from van der Pauw measurements on 200-nm thick sputtered films as noted above.

For Co, Py, and CoFe, our present values of ρ_F agree with prior measurements within mutual uncertainties. For these ferromagnets, we take ρ_F and β_F from those prior studies: $\rho_{Co}=60$ nΩ m (Refs. 7 and 14) and $\beta_{Co}=0.46$ (Ref. 1); $\rho_{Py}=120$ nΩ m and $\beta_{Py}=0.76$ (Ref. 1); and $\rho_{CoFe}=70$ nΩ m and $\beta_{CoFe}=0.65$ (Ref. 15). However, our new measurement of $\rho_{Fe}=100$ nΩ m is much larger than the prior value of $\rho_{Fe}=40$ nΩ m (Ref. 17). In Appendix, we use the technique described in Ref. 13 to estimate $\beta_{Fe}=0.77\pm0.04$ and $l_{sf}^{Fe}=5\pm1$ nm for sputtered Fe with this higher resistivity, and we use these values in our analysis. Note that these new values for Fe differ from those assumed in Ref. 4.

The multilayer data to be analyzed using Eq. (1) are shown in Fig. 1 (top and bottom). Figure 1 (bottom) contains sample hysteresis curves for $n=30$ samples of each F/Al pair. As is often seen in such multilayers,[1] $AR(H)$ is largest at $H=0$ in the as-prepared sample, decreases at high fields to a lowest 'saturation' value of AR^P, and then rises to an intermediate maximum. Since AR^{AP} should be the largest value of AR, we take as our estimates of AR^{AP} the initial (as-prepared) values at $H=0$. In Fig. 1 (top), the data grow linearly with n, as expected from Eq. (1), and the slopes [dominated by $AR_{F/Al}^*$ in Eq. (1)] are large compared to that for the more standard Py/Cu metal pair [filled circles in Fig. 1(a)]. Because AR^{AP} appears in the denominator of Eq. (2), such large values of $AR_{F/Al}^*$ (~10 fΩ m^2) should cause the difference $A\Delta R$ to be relatively small (unless $\gamma_{F/Al}$ is large, which we shall see it is not). After we estimate $\gamma_{F/Al}$ from our EBSVs below, we will calculate the expected sizes of $A\Delta R$ from Eq. (2) and compare the results with data such as those in Fig. 1 (bottom).

For the EBSVs, we focus on $A\Delta R=AR^{AP}-AR^{P}$. With $t_F \gg l_{sf}^F$ (except for Co which has a long spin-diffusion length),

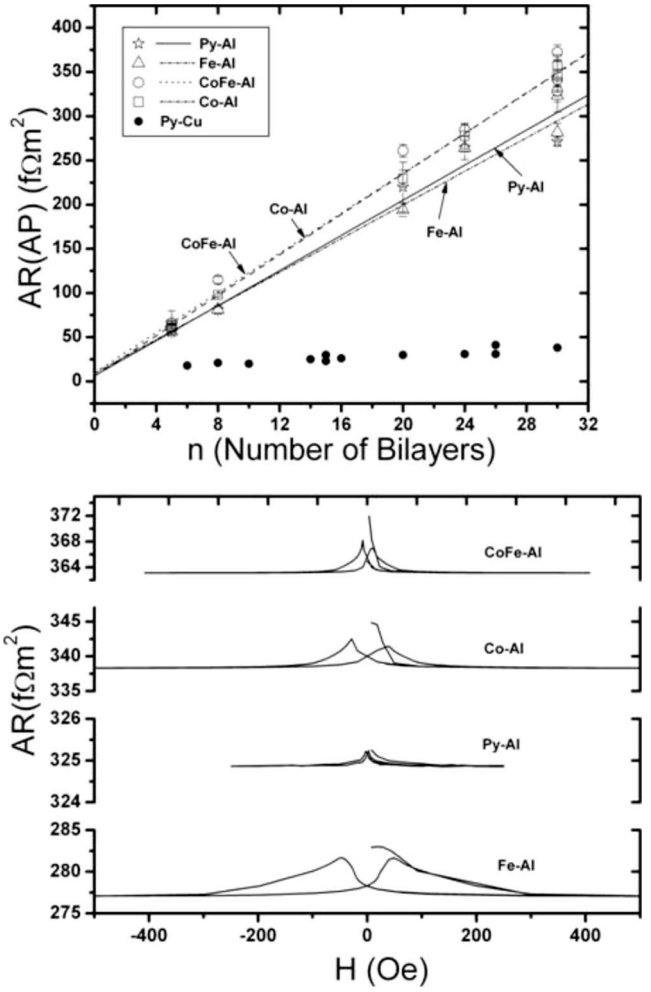

FIG. 1. Top: AR(AP) vs n for F/Al (F=Py,Co,CoFe,Fe) multilayers. Filled circles show, for comparison, data for Py/Cu. Bottom: AR vs H hysteresis loops for some of the $n=30$ multilayers in Fig. 1(a).

we can write the Valet–Fert (VF) equation form in closed form;

$$A\Delta R=4(\beta_F\rho_F^*l_{sf}^F+\gamma_{F/Al}AR_{F/Al}^*)^2/(2\rho_F^*l_{sf}^F+\rho_{Al}t_{Al}+2AR_{F/Al}^*). \quad (3)$$

For Co, we fit the full VF theory numerically, as described in Ref. 13.

Figure 2 (top) shows values of $A\Delta R$ for EBSVs with various values of t_{Al} and Fig. 2 (bottom) shows hysteresis curves for samples with $t_{Al}=10$ nm. We estimate $\gamma_{F/Al}$ by inserting into Eq. (3) the values of the parameters given above plus that of $2AR_{F/Al}^*$ determined from Fig. 1. The resulting estimates of $2AR_{F/Al}^*$, $\gamma_{F/Al}$, and the product $\gamma_{F/A}$ $2AR_{F/Al}^*$ are given in Table I.

Lastly, we checked these values for internal consistency by calculating $A\Delta R$ for the multilayers with $n=30$ and comparing the calculations with the data in Fig. 1(b). For Py/Al, the calculated value of $A\Delta R\sim6$ fΩ m^2 is much larger than the measured $A\Delta R\sim0.5$ fΩ m^2 for $n=30$ in Fig. 1 (bottom). Presumably, as with Py/Cu (Ref. 18), we did not reach a full

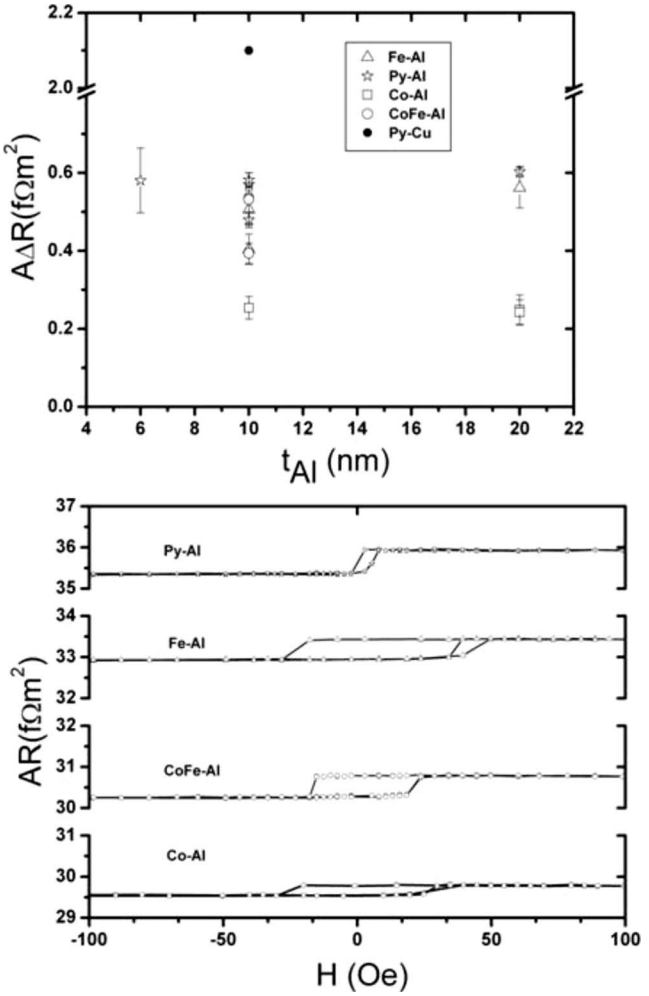

FIG. 2. Top: Comparison of $A\Delta R$ values for $F/\mathrm{Al}(t_{\mathrm{Al}})/F$ (F=Py, Co, CoFe, and Fe) EBSVs. The filled circle shows, for comparison, a value for a Py/Cu/Py EBSV. Bottom: AR vs H hysteresis minor loops for some of the $t_{\mathrm{Al}}=10$ nm EBSVs in Fig. 2(a).

AP state with Py. Increasing our estimate of AR^{AP} to reflect a larger $A\Delta R$ does not significantly affect our estimates of $2AR^{*}_{\mathrm{Py/Al}}$ and thus also of $\gamma_{\mathrm{Py/Al}}$. For CoFe/Al and Fe/Al, the calculated $A\Delta R$s $\sim 6\pm 1$ fΩ m^2 are close enough to the measured values $\sim$6–8 fΩ m^2 in Fig. 1 (bottom) that we have consistency with true AP states. For Co/Al, however, the calculated $A\Delta R\sim 1.5\pm 1$ fΩ m^2 is much smaller than the measured $A\Delta R\sim 7$ fΩ m^2. In this one case, our analysis is not internally consistent. The problem arises from the combination of AR^{AP} and $A\Delta R$ for the Co/Al $n=30$ multilayer that is similar to those for CoFe/Al and Fe/Al (Fig. 1), but an $A\Delta R$ for the Co/Al EBSV that is lower than for the other pairs (Fig. 2). The discrepancy could be due to differences in interfacial structure between the unannealed Co/Al multilayers and annealed Co/Al EBSVs. Such a difference is not unreasonable based upon the diffusion and TEM data given below. But, if so, it is not clear why Co/Al should differ so strongly in this way from the other F/Al pairs studied. Alternatively, the discrepancy might be due to a phenomenon not considered in our analysis, spin-flipping at the F/Al interface. Including such spin-flipping in the VF theory has a much stronger effect on $A\Delta R$ for EBSVs than for multilayers. The combination of an increase in $\gamma_{F/\mathrm{Al}}$ with the presence of a nonzero spin-flipping parameter $\delta_{F/\mathrm{Al}}$, lets $A\Delta R$ increase for the multilayer, while staying fixed for the EBSV at its experimental value. We list as alternative (b) in Table I the resulting values of $2AR^{*}_{\mathrm{Co/Al}}$ (slightly increased) and $\gamma_{\mathrm{Co/Al}}$ (significantly increased), which are coupled with an unexpectedly large value of $\delta_{\mathrm{Co/Al}}\approx 1.8$. If such large spin-flipping at the Co/Al interface is real, it is not clear why there is no need for any spin-flipping at the other F/Al interfaces.

TABLE I. Interface specific resistance ($2AR^{*}$) and scattering asymmetry parameter (γ) for F/Al interfaces.

Metal pair	$2AR^{*}_{F/\mathrm{Al}}$(fΩ m^2)	$\gamma_{F/\mathrm{Al}}$	$\gamma_{F/\mathrm{Al}}2AR^{*}_{F/\mathrm{Al}}$(fΩ m^2)
Py/Al	8.5 ± 1	0.025 ± 0.01	0.21
CoFe/Al	10.6 ± 0.6	0.1 ± 0.01	1.06
Co/Al(a)	11.1 ± 0.2	0.05 ± 0.01	0.56
Co/Al(b)[a]	11.6 ± 0.2[a]	0.18 ± 0.02[a]	2.1[a]
Fe/Al	8.4 ± 0.6	0.05 ± 0.02	0.42

[a]The values listed as (b) are associated with a spin-flip parameter $\delta_{\mathrm{Co/Al}}=1.8\pm 0.5$, see text.

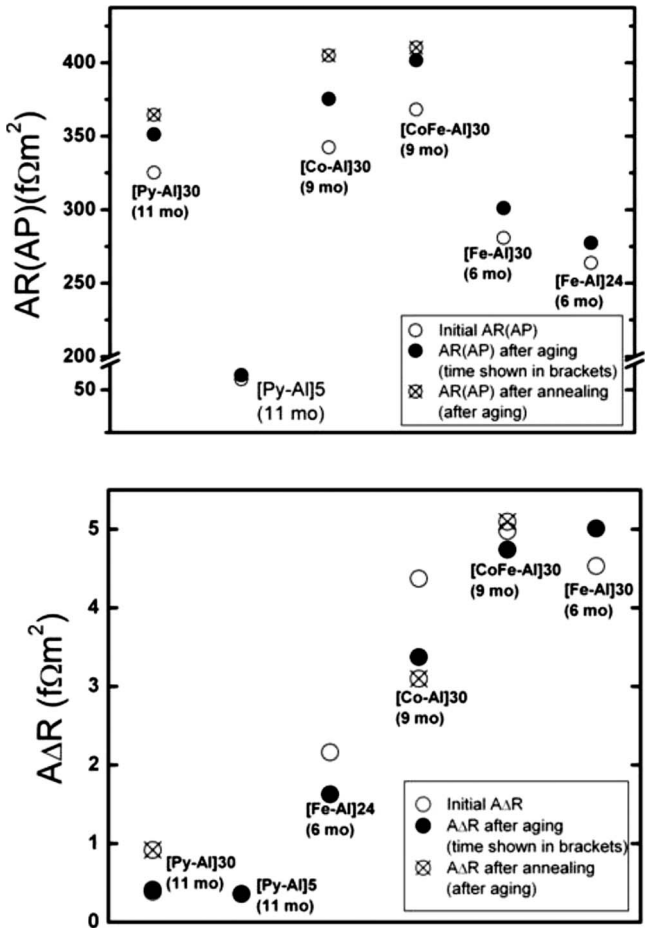

FIG. 3. Effects of aging and annealing on AR(AP) (top) and $A\Delta R$ (bottom) of remeasured F/Al (F=Py, Co, CoFe, and Fe) multilayers. The number of repeats is given after each $[F/N]$.

Figure 3 shows that both AR^{AP} (top) and $A\Delta R$ (bottom)

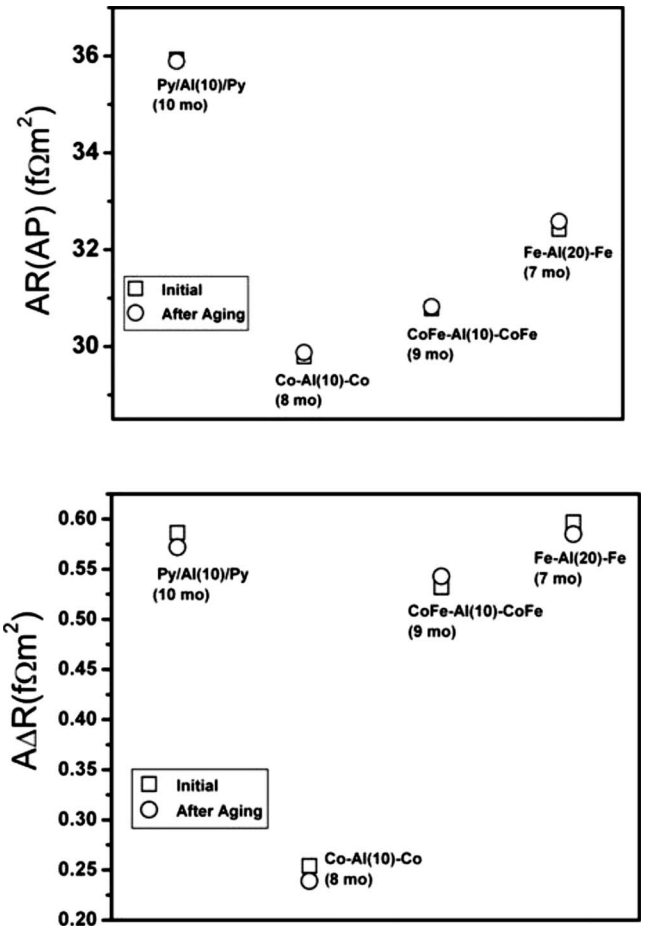

FIG. 4. Effects of aging on AR(AP) (top) and $A\Delta R$ (bottom) of remeasured $F/\mathrm{Al}(t_{\mathrm{Al}})/F$ (F=Py, Co, CoFe, and Fe) EBSVs.

change in selected $n=30$ multilayers and a few others with prolonged time at room temperature and/or with annealing to 450 K. Because the 'initial resistances' in Fig. 1 are not reproduced after the samples are taken to high H saturation, the values of $A\Delta R$ used in Fig. 3 (bottom) are the maximum values after such saturation. Figure 4 shows how AR^{AP} (top) and $A\Delta R$ (bottom) change for selected EBSVs with time at room temperature. We discuss these changes at the end of this section after estimating whether they could be due to interdiffusion of the F and N metals. To do this, we must estimate the diffusion constants $D(T)$ for bulk motion of the F-metals of interest into Al and vice versa at the temperatures of present interest, 300 and 450 K. Since the data for such interdiffusion have been taken only at much higher temperatures[19] and only for dilute concentrations of the diffusing atoms, we must extrapolate from these higher temperatures to 300 and 450 K and assume that the resulting coefficients can be used for our samples where the concentrations for interdiffusion are not dilute. Moreover, our sputtered multilayers grow as columnar polycrystals, with columns ~20–40 nm in diameter (see Figs. 5–7, 14, and 15 below). At our lower temperatures, mass transport might be dominated by diffusion along the column boundaries. Our estimates of bulk diffusion are, thus, likely to be only lower bounds on the actual diffusion rate.

TABLE II. Estimated diffusion distances d(nm) in 1 min at 300 and 450 K for dilute concentrations of metal one in two.

1 in 2	d(nm) for 1 min	
	300 K	450 K
Al in Ni	4×10^{-15}	1×10^{-7}
Ni in Al	7×10^{-5}	1
Al in Fe	3×10^{-12}	1×10^{-5}
Fe in Al	8×10^{-8}	2×10^{-2}
Co in Al	2×10^{-6}	2×10^{-1}

We assume the standard Arrhenius form $D(T)=D_o\exp(-Q/\mathrm{k}T)$ where D_o is the prefactor in units of $\mathrm{m/s}^2$, Q is the activation enthalpy for diffusion in eV/atom, k is Boltzmann constant, and T is the absolute temperature. To estimate the distances that each metal can diffuse into the other, we use the standard one-dimensional diffusion equation;

$$d=\sqrt{4D_o t\,\exp(-Q/kT)}, \tag{4}$$

where t is the diffusion time. Table II lists our estimates of d for $t=1$ min at 300 and 450 K. When more than one pair of D_o and Q was given in Ref. 19, we list for d the linear average of the resulting values of d at either 300 or 450 K. Due to typical variations in these values and uncertainties in the extrapolations, we list d to only one significant figure and we view the uncertainty in each d as at least a factor of two. The distance diffused in one year can be estimated by multiplying a listed value by 0.72×10^3. We find that dilute concentrations of all of the F-metals under study diffuse significantly into bulk Al at 450 K in minutes but do not diffuse significantly into bulk Al at 300 K even in a year. Dilute Al does not diffuse into any of the bulk F-metals at either temperature in a year. Of course, with the high concentrations of F and Al near our F/Al interfaces, diffusion of F into Al requires at least some counter diffusion of Al into F.

The possibility of interdiffusion of F-metals into Al (and vice versa), just described (given, as noted, that the estimates of interdiffusion above are likely to be lower bounds), stimulated us to remeasure a representative subset of our samples after aging for 6–11 months at 295 K and after annealing at 450 K for ~1 min. For comparison, we note that multilayers and EBSVs that we have studied over the years, which contain N-metals other than Al, retain their same resistances to within 1% or less after years at 295 K or after annealing to 450 K, and their values of $A\Delta R$ are also stable. In contrast, for those multilayers with Al that we remeasured, Fig. 3 shows that AR(AP) grows by 5%–10% after 6–11 months and by a further 2%–7% upon annealing to 450 K. The values of $A\Delta R$ often change by even larger fractions but sometimes decrease and sometimes grow. For the remeasured EBSVs containing Al, in contrast, which were already heated to 450 K in processing, Fig. 4 shows that both AR^{AP} and $A\Delta R$ change by much smaller amounts than for the multilayers.

In Sec. IV, we describe what we learned when we compared TEM, HRTEM, and EELS studies of as-sputtered and annealed samples of Co/Al and Py/Al.

TABLE III. Lattice parameters and close-packed interplanar spacing variants for the multilayers. $d\mathrm{Si}_{002}=0.272$ nm is used as reference.

Materials	Lattice parameters (nm)	Interplanar spacings measured for (111)	Interplanar spacings for (111) in theory
Al	$a_0=0.405$	0.235 ± 0.002 nm	0.234 nm
Co	$a_0=0.251$, $c_0=0.407$ (hcp)	N/A	N/A
	$a_0=0.356$ (fcc)	0.205 ± 0.002 nm	0.206 nm
Py (NiFe)	$a_0=0.355$	0.204 ± 0.002 nm	0.205 nm

IV. TRANSMISSION ELECTRON MICROSCOPY, HIGH RESOLUTION TRANSMISSION ELECTRON MICROSCOPY, AND ELECTRON ENERGY LOSS SPECTROSCOPY STUDIES OF Co/Al AND Py/Al

We present detailed TEM, HRTEM, and EELS studies of Co/Al and Py/Al as representatives of the F/Al structures of interest. We were especially interested in trying to answer the following questions: (1) Do the sputtered Py (fcc), Al (fcc), and Co (faulted mixture of fcc and hcp) layers all have their equilibrium crystal structures and the expected (111) orientations normal to the layer planes? (2) How do the F and Al layers, with their different lattice parameters, connect at the F/Al interfaces? (3) Do the F and Al significantly intermix and/or form intermetallic phases?[20] (4) Of particular interest for potential changes in R and ΔR with time or annealing, how thick are the interfaces and do they broaden upon annealing? A partial TEM, HRTEM, and EELS study of these multilayers was presented in Ref. 21 from which we repeat one white line intensity figure on Co/Al—Fig. 13—so that the reader may conveniently compare those results with related ones for Py/Al in Fig. 17.

Magnetic multilayers of the form $[F(20)/N(10)]_{10}$, with 10 Co(or Py)/Al bilayers, were grown on the same Si(100) substrates as our samples for resistance studies. They were also grown at the same low temperature (from 243 to 273 K) using the same dc-magnetron triode sputtering system with a base pressure $\sim 2\times 10^{-8}$ torr. For comparison with the as-sputtered samples, some multilayers were annealed after sputtering at 450 K for less than 5 min in the same chamber.

Cross-sectional TEM samples were prepared using the sandwich technique by joining the multilayers face-to-face and sectioning along a $\langle 110\rangle$ direction lying in the (001) surface plane in the Si substrates. *M*-bond™ 610 epoxy, cured at room temperature for long time (i.e., 24 h), was used to form the sandwiches. The sections were bonded to a preheated sapphire flat (~353 K) using crystal bond™ wax to facilitate mechanical polishing and dimpling. Upon removal from the hot plate, the wax solidifies in a matter of seconds. The total time that the samples remained at 353 K was less than 5 s. Following dimpling, the samples were removed from the sapphire flat using acetone. Final thinning was carried out using a Gatan PIPS ion mill at ~4° angle.

The structures of individual layers and interfacial regions were studied by HRTEM with associated fast Fourier transforms (FFT). Selected area diffraction (SAD) patterns were obtained using circular apertures that allowed information to be collected across the breadth of the multilayers and a portion of the Si substrates. To complement these studies, spatially resolved EELS was performed in conjunction with scanning transmission electron microscopy (STEM) to characterize the interfacial regions. HRTEM and EELS were carried out at 200 kV using a JEOL JEM-2200FS (TEM/STEM) with in-column omega energy filter. EELS spectrum images (a series of spatially resolved EELS spectra) were collected by scanning an ~0.5 nm diameter [full width at half maximum (FWHM)] probe across the interfaces of the F/N multilayers. Each spectrum was composed of 1024 EELS channels of 0.11 eV width. Low loss spectrum images with plasmon peaks were acquired over scans of ~50 nm across $F/N/F/N/F$ layers. Core loss spectrum images with white lines for Co (or Ni, Fe) were acquired using scans of ~20 nm across $F/N/F$ layers. During the acquisition process, specimen drift caused by thermal effects was corrected using Gatan DigitalMicrograph® by periodically scanning over a cross-correlated reference region in the survey images.

We expected the layers to grow as close-packed planes with fcc (111) normals (except for Co, which grows as faulted fcc and hcp—see below). Table III shows that the measured interplanar layer separations agree with the values expected for bulk metals to within experimental uncertainties.

In the following, TEM and HRTEM images are representative of images at several places along the thinned part of each multilayer. Each EELS spectrum is representative of 3–5 scans.

A. Details of as-sputtered and annealed Co/Al multilayers

We started our study of the effect of annealing upon Co/Al multilayers with simple phase contrast TEM studies. Figure 5 shows a phase contrast cross-sectional TEM image of an as-sputtered Co/Al multilayer and Fig. 6 shows a similar image of an annealed Co/Al multilayer. In both cases, the Co and Al layers are well layered, polycrystalline, and their thicknesses are consistent with the nominal 20 nm Co and 10 nm Al. In-plane grain sizes are ~20 nm and no obvious intermediate phases are observed. Both pictures show significant layer roughness, in the form of nonplanar interface perturbations, resulting in the interfacial planes lying as much as 15° from the growth plane. SAD patterns from both the multilayers and Si substrates (see insets) show strong diffraction for the close-packed planes of Co and Al in the growth direction, indicating that the layers are highly textured.

Due to a low stacking fault energy, sputtered or evaporated Co layers generally contain faulted mixtures of fcc and

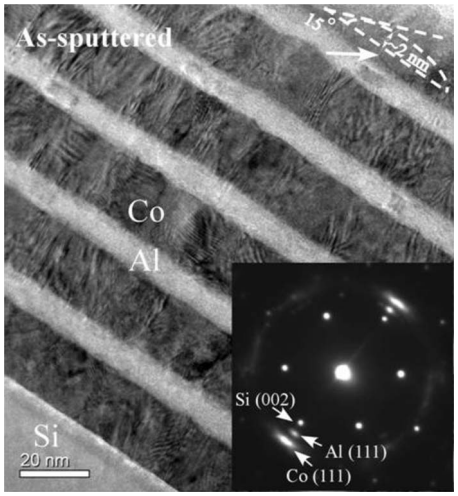

FIG. 5. A phase contrast TEM image of an as-sputtered Co(20)/Al(10) multilayer on a Si substrate. The Inset shows a selected area diffraction pattern from both the multilayer and Si substrate displaying strong diffraction of close-packed growth plane of both Co and Al parallel with Si(001). On the upper right, an inclined grain is illustrated schematically to show that the waviness perpendicular to the electron beam is up to 2 nm at the interfaces.

hcp layers.[22–24] Since stacking faults have been found to affect the current-in-plane (CIP)-MR,[25] it is important to characterize the crystal structures and faulting of the Co in our multilayers. Figure 7(a) shows an HRTEM image of all three layers of an as-sputtered Co/Al/Co sample, where the Co and Al layers are clearly distinguished. Two Al grains are resolved in the light contrast layer, revealing a ~7° angle between the two Al(111) growth planes. Within the Co layers, the atomic structure is resolved but somewhat obscured by the Moiré fringes, caused by overlapping grains in the beam direction. The FFT (see inset) shows two strong Al diffraction spots from {111} close-packed planes but a variety of Co diffraction spots from both fcc and hcp regions. Since the image is not taken from a well aligned Co crystal zone (as

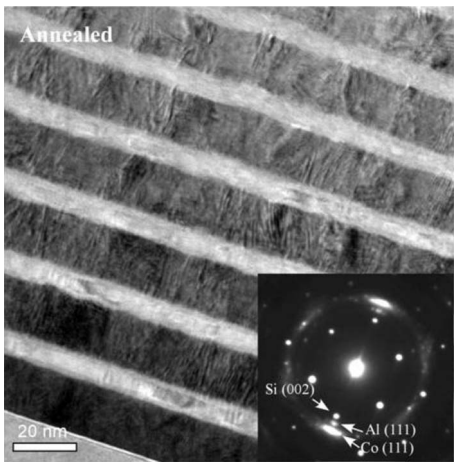

FIG. 6. A phase contrast TEM image of an annealed Co(20)/Al(10) multilayer. The inset shows an SAD pattern with strong {111} reflections in the growth direction, indicating growth on the close-packed planes.

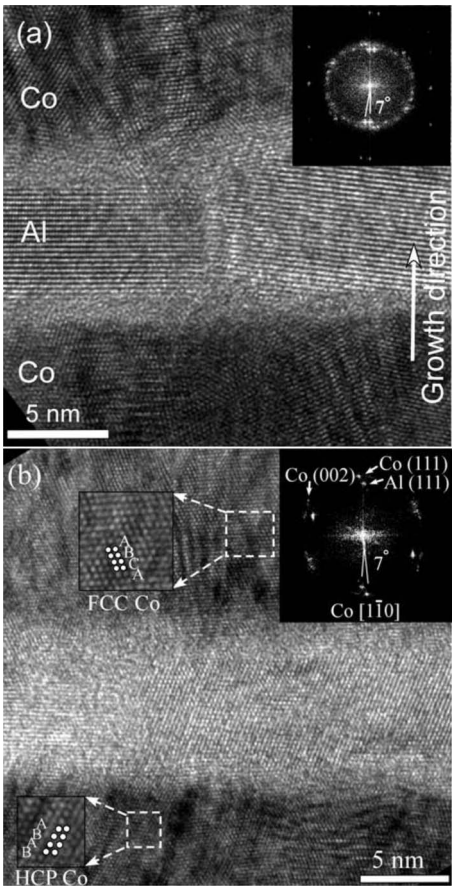

FIG. 7. HRTEM images show atomic resolution in the Co and Al layers. The Co/Al interfaces are poorly defined. A grain boundary in the Al is observed in (a). Both fcc and hcp stacking are shown in (b) in Co imaged along ⟨110⟩. Insets in the upper right show FFTs from the images displaying the misorientation between the Co and Al close-packed planes.

indicated by the inset FFT), the Co close-packed plane stacking is not clearly defined. Figure 7(b) shows another area from this multilayer with both the Al and Co clearly resolved. Most of the Co in this image displays a $\langle 110 \rangle_{FCC}$ zone axis with fcc *ABCABC* stacking of the close-packed {111} planes (see upper inset). Nevertheless, some hcp *ABAB* stacking was also seen (see lower inset). Analysis of several different areas showed that fcc stacking dominates over hcp. An interesting feature is that their ~14% different lattice parameters caused the close-packed {111} Al (fcc) and Co (fcc) planes to not form coherent {111} interfaces. Instead, a significant angular deviation ~7° is found between the $\{111\}_{Al}$ and $\{111\}_{Co}$ plane normals, as illustrated in the FFT inset in Fig. 7(b). Although such deviations were most evident in grains imaged in the ⟨110⟩ orientation, they were seen consistently along the interfaces.

Unfortunately, the interfaces of the Co/Al layers in Fig. 7 and other such pictures were somewhat obscured, making it difficult to identify any intermetallic phases that may have formed by interdiffusion. However, a through-focus series of images (Fig. 8) can help to clarify the interfacial structure along the electron beam. The four images were taken from the same area but at relative defocuses of 0, 32, 64, and 96

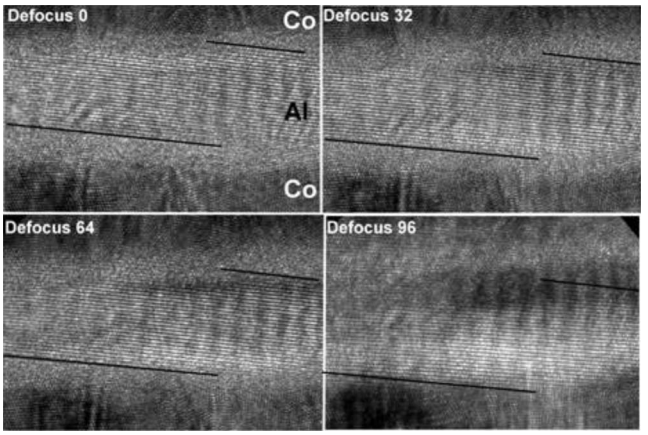

FIG. 8. A through-focus series of images from the same area of the multilayer shows lattice fringe contrast in the Al and Co varying with defocus indicating the Al/Co interfaces are inclined along the beam direction.

nm (note, these values do not indicate the actual depth into the sample, which we estimate at only ~10 nm). For a defocus of zero, the Al stacking extends through the interfacial region and to the Co at the upper interface. As the defocus is changed, this distinct stacking of Al planes becomes obscured at the upper interface but extends closer to the lower interface until it finally reaches the Co layer. HRTEM image simulations show that at different defocuses lattice fringes from a Ni_3Al crystal will terminate at different positions relative to an inclined grain boundary.[26,27] Thus, this through-focus series suggests that what appears to be an interfacial region between the Co and Al is actually, at least partly, the result of the interfaces being inclined to the electron-beam direction. If, from Figs. 5–7 we estimate 'blurred' interfacial regions of width 2–2.5 nm, then the tilting in Fig. 7 suggests that the physically mixed region is actually only 1–1.5 nm. We take this 1–1.5 nm as a lower bound on the interface width since it neglects any possible chemical intermixing of Co and Al atoms in the 'perfect' crystallites on both sides of the mixed region. We will use EELS measurements below to set upper bounds.

Given the observed interface and layer roughness perpendicular to the electron beam of approximately 2 nm over a width of 20 nm illustrated in Figs. 5 and 6, one would also expect the interfaces to exhibit some waviness in the electron-beam direction. With a TEM foil thickness ~10 nm, and an assumed interfacial region thickness ~1–1.5 nm, the interfacial waviness in the electron-beam direction is consistent with the interfacial waviness perpendicular to the electron-beam direction. Figure 9 shows a schematic model of Al{111} growing on Co{111}. The mismatch between the two lattices, calculated from the lattice parameters of fcc Al and Co listed in Table II, is 13.7% for Al{111} growing on Co{111}. Clearly, it is unlikely that these layers will directly heteroepitax on each other. Instead, the mismatch looks to be accommodated by significant tilting between those lattices (Fig. 9), resulting in inclined interfaces and apparent roughness.

Figure 10(a) shows a high angle annular dark field STEM image of the as-sputtered Co/Al multilayers. The contrast is

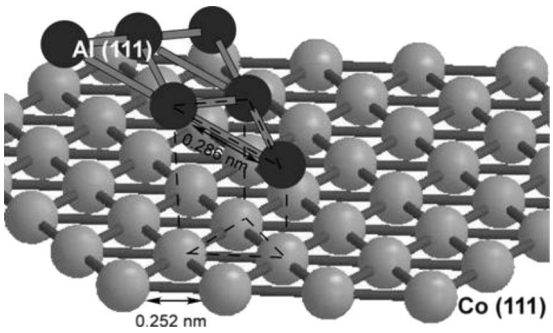

FIG. 9. Schematic model illustrating the tilting of the fcc Al {111} on fcc Co {111} growth planes resulting from a lattice mismatch of 13.7%

proportional to Z^2, so the Co ($Z=27$) layers are much brighter than the Al ($Z=13$) layers. A set of EELS spectra was collected by line scanning the electron probe across layers. Figure 10(b) shows a perspective view of an EELS spectrum image with 61 regularly spaced low loss spectra ob-

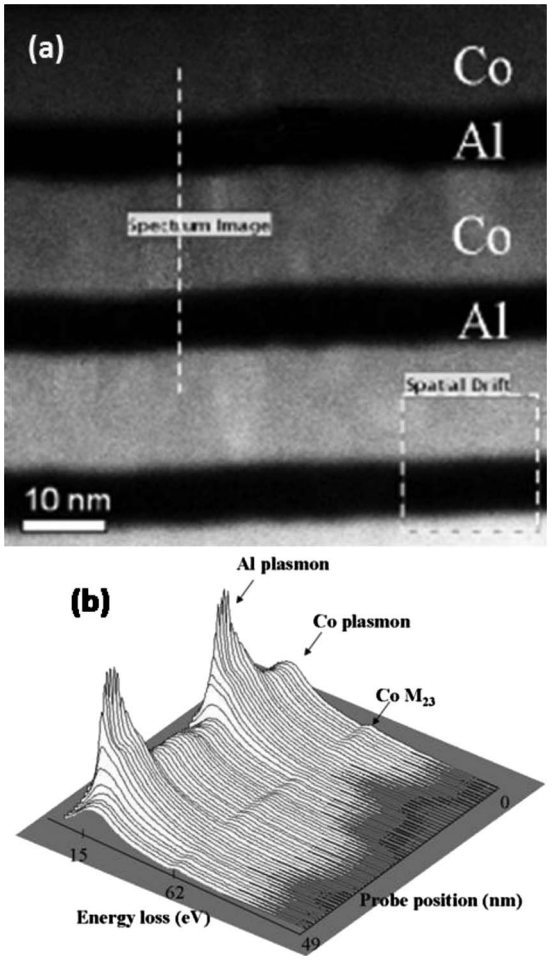

FIG. 10. (a) A dark field STEM image of an as-sputtered Co/Al multilayer in which an EELS spectrum image was acquired along the white dashed line. The spatial drift square shows the cross-correlation scan area used to correct for TEM sample drift. (b) A perspective view of the EELS spectrum image shows that the plasmon intensity changes across the Co/Al multilayer.

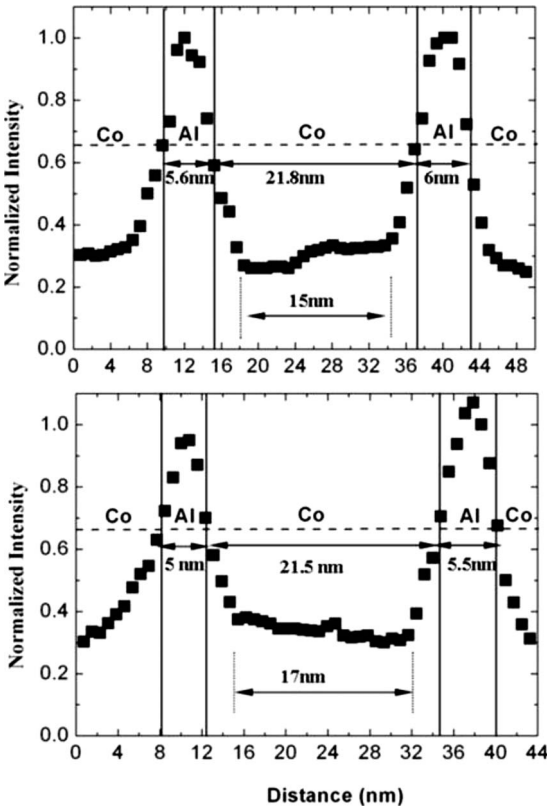

FIG. 11. A comparison of plasmon intensity profile for as-sputtered (top) and annealed (bottom) Co/Al multilayers. The Al plasmon peak profile exhibits a similar full width at half maximum of 5–6 nm for both the as-sputtered and annealed samples. The only notable difference is that the low variation portion of the Co intensity is 15 nm long for the as-sputtered multilayer and 17 nm long for the annealed multilayer.

tained along the 49 nm line indicated in Fig. 10(a). The square frame labeled "spatial drift" indicates the area used as the reference to correct the specimen drift during the spectra collection. It is known that Al has a very intense plasmon peak compared to many metals, including Co, Fe, and Ni (Ref. 28). Thus, the low loss spectrum of plasmon intensities can give an indication of the elemental distribution across the spectrum image. Figure 11 shows a comparison of plasmon intensity profiles for as-sputtered and annealed Co/Al multilayers. Both plasmon peak profiles across the Al-rich layers are 5–6 nm in FWHM, indicating similar Al distributions in the as-sputtered and annealed samples. Within the Co-rich layers, relatively constant regions, approximately 15 nm wide for the as-sputtered multilayer and 17 nm wide for the annealed multilayer, suggests there are no significant differences in the Co distribution in the two conditions.

An alternative way to characterize interfacial compositions using EELS is to investigate the Co L_{23} edge intensity profile across Co/Al interface, which can provide sufficient insight in the chemical nature at the Co/Al interfacial region. Figure 12 shows a perspective view of EELS spectrum image recorded around the Co L_{23} edge (L_3:779 eV and L_2:794) across Co/Al/Co layers for an as-sputtered sample. Upon removing a power-law background for each spectrum, the intensities of L_3 peaks are analyzed in Fig. 13 (shown as

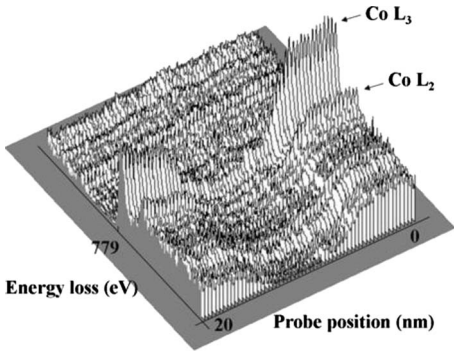

FIG. 12. A perspective view of the Co white line intensity profile from a 20 nm scan across an as-sputtered Co/Al/Co multilayer.

open circles). This is compared to a similarly processed intensity profile for the annealed layers (solid squares in Fig. 13). To facilitate an understanding of the two experimental profiles, a theoretical Co intensity profile across perfect Co/Al/Co interfaces (see in Fig. 13) has been simulated using an electron beam with a 0.5 nm (FWHM) Gaussian profile. The experimental data reveal significantly broader interfacial mixing than the theoretical profile for a perfect (unmixed interface). From Figs. 11 and 13 we estimate an upper bound on the interface width of 2.5–3 nm. Some of the observed broadening will be associated with the inclination of the interfaces described earlier and some will be due to beam divergence and to spreading in the TEM thin foil (both ignored in the simulation). Unfortunately, estimating the latter phenomena is difficult and beyond our capabilities. We can, thus, only conclude that the interfacial mixing is not smaller than 1 nm or larger than 3 nm. Our TEM and FFT images show no evidence of additional phases; the structures of the intermetallic phases present in the Co-Al binary phase diagram differ enough from those of Al (fcc), Co (hcp or fcc), and Si that their presence would have generated additional FFT spots.

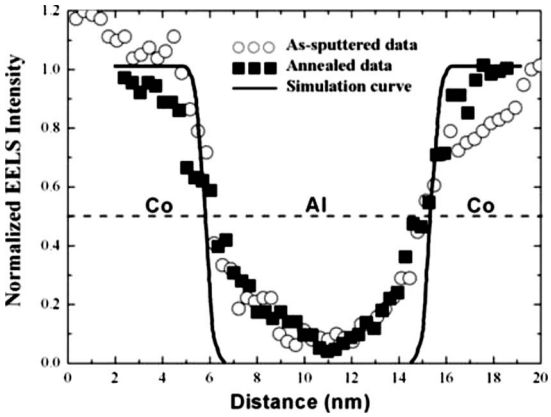

FIG. 13. Co white line intensity profiles for both as-sputtered (open circles) and annealed (filled squares) multilayers. A theoretical profile, simulated by adding a 0.5 nm FWHM Gaussian electron beam profile to perfect Co/Al interfaces, is shown for comparison to the experimental data. From Ref. 21.

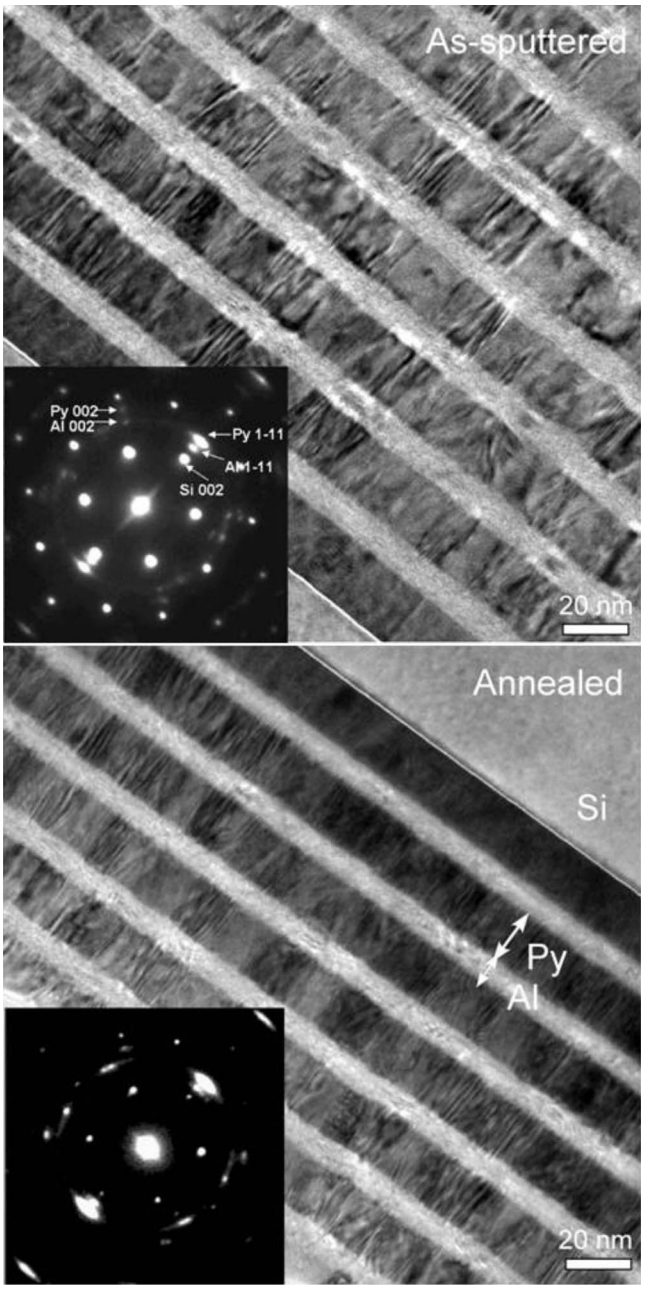

FIG. 14. Phase contrast TEM images of an as-sputtered (bottom) and annealed (top) Py(20)/Al(10) multilayers. Insets show selected area diffraction patterns from the multilayers. Together, the morphologies and diffractions from Py(111) and Al(111) show similar layer structures.

B. Details of as-sputtered and annealed Py/Al multilayers

Phase contrast TEM images of both as-sputtered and annealed Py/Al multilayers grown on Si are shown in Fig. 14. As with Co/Al, the images reveal the layers to be polycrystalline, while the strong diffraction peaks in the growth direction for the close-packed Py and Al{111} planes in the SAD patterns (see the insets in Fig. 14) show that Py and Al are highly textured. The thicknesses of the individual layers are consistent with the nominal 20 nm Py and 10 nm Al. The Py had grains with sizes in the range of ~20 nm and, similar

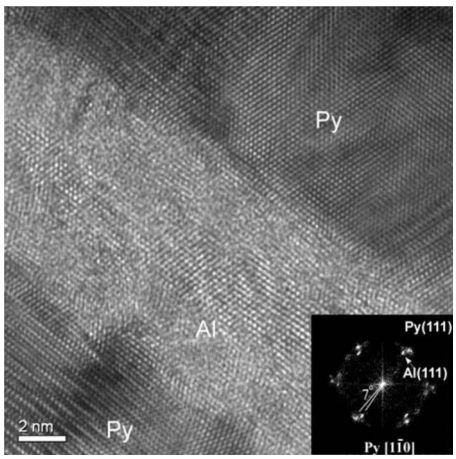

FIG. 15. An HRTEM image of an annealed Py/Al multilayer along a Py ⟨110⟩ zone. The corresponding FFT in the inset shows the growth relationship.

to the Co/Al multilayers, some of the interface normals are tilted. The layer structures and interface roughness do not reveal any obvious differences between the as-sputtered and annealed samples.

Figure 15 shows an HRTEM image of an annealed Py/Al multilayer with most of the Py and some of the Al clearly resolved. *ABCABC* stacking of the close-packed $\{111\}_{FCC}$ planes are displayed in both Py and Al. The FFT (see lower inset) shows that the grains are imaged along $\langle 110\rangle_{FCC}$ zones of Py and Al. Again, a significant angular deviation of 7° between the $\{111\}_{\mathrm{Al}}$ and $\{111\}_{\mathrm{Py}}$ plane normals is found, which will lead to incoherent interfaces. Likewise, the lattice fringes are obscured near the interfaces of the Py/Al layers in the image, which again can be interpreted as resulting from inclined interfaces.

It is known that both Fe and Ni can form a range of intermediate phases with Al, including several ternary intermediate phases.[29] To see if any intermediate phases formed at the Py/Al interfacial region in the as-sputtered and annealed multilayers, we used spatially resolved EELS to study the composition across the interfaces. EELS spectrum images that included the low-energy plasmon and Ni and Fe *L* edges (Ni L_3:855 eV and Fe L_3:708 eV), were collected across the interfaces. Figure 16 compares the normalized plasmon intensity profiles of across Py/Al/Py/Al/Py layers, which reveal layer thicknesses consistent with the nominal thicknesses. Figure 17 compares intensity profiles of Ni (a) and Fe (b) at the interfaces of the Py/Al/Py layers with simulated theoretical profiles. No significant differences are observed between the annealed and as-sputtered Py/Al/Py profiles, suggesting that annealing did not significantly alter the multilayer structure. Nevertheless, the widths of the intensity profiles do suggest that some compositional mixing occurs during the initial growth.

C. Answers to posed questions

(1) Do the sputtered Py (fcc), Al (fcc), and Co (faulted mixture of fcc and hcp) layers all have their equilibrium

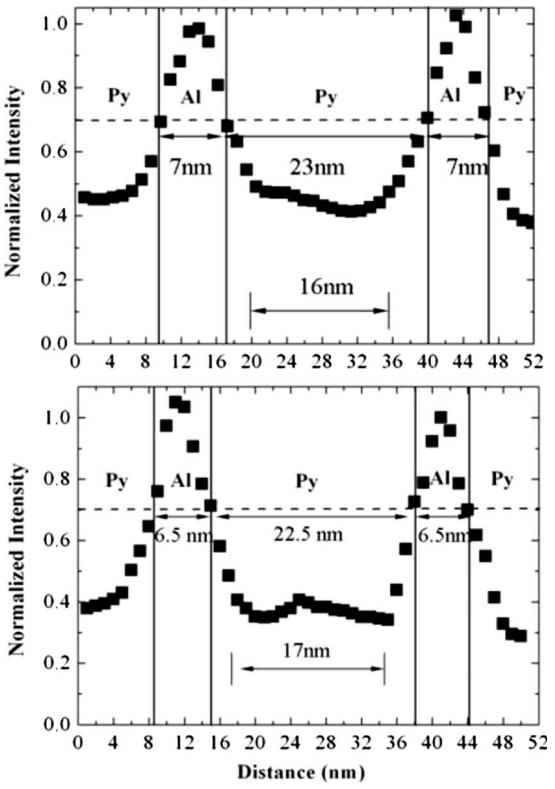

FIG. 16. A comparison of plasmon intensity profiles for as-sputtered (top) and annealed (bottom) Py/Al multilayers. The Al plasmon peak profiles exhibit similar shapes, with full widths at half maximum of 6–7 nm, for both as-sputtered and annealed samples.

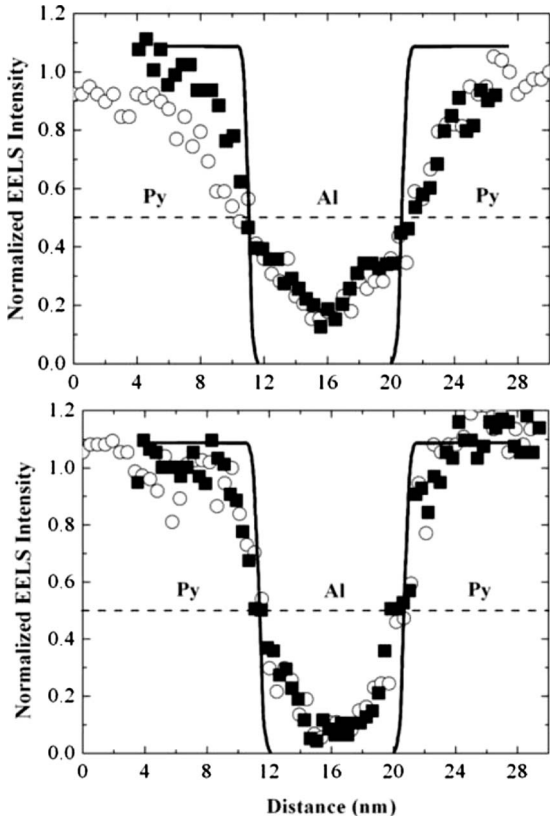

FIG. 17. Ni (top) and Fe (bottom) white line intensity profiles for as-sputtered (open circles) and annealed (filled squares) multilayers are compared separately with the theoretical profile simulated by adding a 0.5 nm FWHM Gaussian electron-beam profile to perfect Py/Al interfaces.

crystal structures and the expected (111) orientations normal to the layer planes? Yes.

(2) How do the F and Al layers with different lattice parameters connect at the F/Al interfaces? They connect with some misfitting, resulting in incoherent interfaces with nonparallel close-packed planes.

(3) Is there evidence of significant intermixing of the F and Al and/or formation of intermetallic phases? We find evidence for intermixing over at least 1 nm but not more than 3 nm, but no evidence of intermetallic phases.

(4) Of particular interest for potential changes in R and ΔR with time or annealing, how thick are the interfaces and do they broaden upon annealing? Interface tilting and beam divergence and spreading, limit our ability to pin down an intrinsic width. We can only set limits greater than 1 nm but less than 3 nm. We can, however, say that the width does not significantly broaden upon annealing.

V. SUMMARY AND CONCLUSION

We used our standard CPP-MR techniques on a combination of multilayers and exchange biased spin valves to derive interface parameters $2AR^*_{F/\mathrm{Al}}$ and $\gamma_{F/\mathrm{Al}}$ for F/Al interfaces (F=Py, Co, CoFe and Fe). In all four cases, we found large values of $2AR^*_{F/\mathrm{Al}}$=8.4–11.6 fΩ m^2 but small values of $\gamma_{F/\mathrm{Al}} \leq 0.18$. In one case, Co/Al, we find possible evidence of spin-flipping at the Co/Al interface but no such evidence for any of the other three F/Al pairs. Holding the multilayers at 293 K for several months or annealing them at 450 K for a few minutes produced changes in both total AR and $A\Delta R$ $\sim$5–10%, large enough to indicate modest structural changes. Similar holding or annealing of EBSVs showed smaller changes in either AR or $A\Delta R$, probably because the EBSVs had already been annealed at 450 K during pinning. Detailed TEM, HRTEM, and EELS studies of separately prepared F/Al multilayers showed that the samples are well layered and grow with both F and Al metals having their bulk structures and with the growth direction normal to the close-packed planes. There was intermixing at the F/Al interfaces over distances $\sim$1 nm but no evidence of intermetallic phase formation. The intermixing did not seem to increase significantly upon annealing to 450 K.

A potential reason for the large measured values of $2AR^*_{F/\mathrm{Al}}$ might be interfacial alloying. Taking resistivities of dilute alloys of F in Al or Al in F as $\sim$20–60 nΩ m/at. % [30] and multiplying by 25 to get an approximate 50%–50% alloy $[c(1\text{-}c)=(50\times 50)/100=25]$ gives $\rho_{\mathrm{Alloy}} \leq 1.5 \times 10^{-6}$ Ω m. To obtain $AR \approx 5$ fΩ m^2 requires multiplying this ρ_{Alloy} by an alloy thickness, $t_{\mathrm{Alloy}} \geq 3$ nm, at the upper limit of our estimate of interface width. It would, thus, be helpful to have calculations of the interface resistances for Co/Al and Py/Al to see how much of them can be attributed

to band-structure mismatch between the F and Al metals. Having found such large values of $2AR^*_{F/\mathrm{Al}}$, even though with small $\gamma_{F/\mathrm{Al}}$, gives hope that there might exist other F/N pairs with large values of both parameters that would be superior for devices to present metal pairs such as Py/Cu or Co/Cu.

ACKNOWLEDGMENTS

This work was supported in part by the NSF through Grants No. DMR-05-01013 and No. DMR-03-05472 and the JEOL 2200 FS used in this study was supported in part through NSF Grant No. DMR-00-79578.

APPENDIX: ESTIMATING β_{Fe} AND $\ell_{\mathrm{sf}}^{\mathrm{Fe}}$ FOR OUR SPUTTERED Fe

In Sec. III, we noted that: (a) the resistivity of the present Fe (100 nΩ m) is much higher than that (40 nΩ m) in a prior study[17] and (b) the parameters that we use in the present study differ from those that we used in Ref. 4. We are not sure why the present resistivity is so much higher but the new and old Fe sputtering targets appear to be from different manufacturers and to be dominated by different impurities. In Ref. 4, as we had no other information available, we estimated β_{Fe} and $\ell_{\mathrm{sf}}^{\mathrm{Fe}}$ by assuming particular scalings for each. For the present paper, we removed the need for these assumptions by performing additional measurements.

A sputtered alloy such as Py, where scattering is dominated by a known concentration of a known impurity (Fe), should have a unique residual resistivity and unique CPP-parameters at 4.2 K. In contrast, for a sputtered layer of a nominally 'pure' bulk metal such as Fe or Co, the dominant scatterers are an unknown combination of unknown impurities. Hence, neither the residual resistivity nor the CPP-MR parameters should be unique at 4.2 K; rather, the latter should vary with the residual resistivity and perhaps also with the details of the impurities present. We have spent over a decade showing that, so long as the residual resistivities of test layers of a pure metal sputtered in our system remain closely the same, the CPP parameters of that metal usually stay the same to within uncertainties of 10%–20%.[1] Thus, once we found a different residual resistivity for our sputtered 'new' Fe, for the most reliable analysis, we had to measure β_{Fe} and $\ell_{\mathrm{sf}}^{\mathrm{Fe}}$ for layers of this new Fe sputtered with the same system and in the same way as was used to make the multilayers in the present experiments, hence, this appendix.

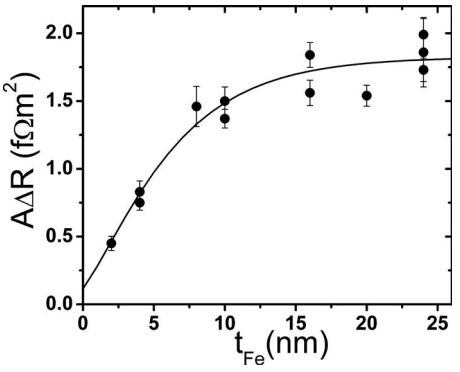

FIG. 18. $A\Delta R$ vs t_{Fe} for EBSVs with variable thickness t_{Fe} of the two Fe layers.

We estimate β_{Fe} and $\ell_{\mathrm{sf}}^{\mathrm{Fe}}$ for our sputtered Fe using the Valet–Fert theory and the technique described in Ref. 13. Figure 18 shows a plot of $A\Delta R$ vs t_{Fe} for a set of $[\mathrm{FeMn}(8)/\mathrm{Fe}(t_{\mathrm{Fe}})/\mathrm{Cu}(10)/\mathrm{Fe}(t_{\mathrm{Fe}})]$ exchange-biased spin-valves with variable thickness t_{Fe} of the two Fe layers. The ordinate intercept is determined by the interfacial parameters $2AR^*_{\mathrm{Fe/Cu}}=1.48\pm0.14$ fΩ m^2 and $\gamma_{\mathrm{Fe/Cu}}=0.55\pm0.07$ taken from Ref. 31—i.e., we assume that the Fe/Cu interface is insensitive to differing residual impurities in the Fe and Cu. Taking $\rho_{\mathrm{Fe}}=100$ nΩ m from measurements on sputtered thin Fe films and Nb/Fe/Nb multilayers,[4] we fit the data of Fig. 18 using β_{Fe} and $\ell_{\mathrm{sf}}^{\mathrm{Fe}}$ as the only unknown parameters. The fit shown gives $\beta_{\mathrm{Fe}}=0.77\pm0.04$ and $\ell_{\mathrm{sf}}^{\mathrm{Fe}}=5\pm1$ nm. This value of $\beta_{\mathrm{Fe}}=0.77\pm0.04$ overlaps with the β_{Fe} for the lower resistivity Fe in Refs. 17 and 31 and the ratio $(5\pm1)/(8.5\pm1.5)=0.59\pm0.16$ of the present and former[31] values of $\ell_{\mathrm{sf}}^{\mathrm{Fe}}$ just overlaps with that $(40\pm10)/(100\pm10)=0.4\pm0.11$ of the former and present resistivities (see Ref. 4).

[1] J. Bass and W. P. Pratt, Jr., J. Magn. Magn. Mater. **200**, 274 (1999).
[2] A. G. F. Garcia, I. N. Krivorotov, P. M. Braganca, D. C. Ralph, and R. A. Buhrman, Bull. Am. Phys. Soc. **50**, 237 (2005).
[3] N. Theodoropoulou, A. Sharma, R. Loloee, W. P. Pratt, Jr., J. Bass, A. Fert, and H. Jaffres, J. Appl. Phys. **99**, 08G502 (2006).
[4] N. Theodoropoulou, A. Sharma, T. Haillard, R. Loloee, W. P. Pratt, Jr., J. Bass, J. Zhang, and M.A. Crimp, IEEE Trans. Magn. **43**, 2860 (2007).
[5] S.-F. Lee, W. P. Pratt, Jr., Q. Yang, P. Holody, R. Loloee, P. A. Schroeder, and J. Bass, J. Magn. Magn. Mater. **118**, L1 (1993).
[6] T. Valet and A. Fert, Phys. Rev. B **48**, 7099 (1993).
[7] J. Bass and W. P. Pratt, Jr., J. Phys.: Condens. Matter **19**, 183201 (2007).
[8] J. M. Slaughter, W. P. Pratt, Jr., and P. A. Schroeder, Rev. Sci. Instrum. **60**, 127 (1989).
[9] S.-F. Lee, Q. Yang, P. Holody, R. Loloee, J. H. Hetherington, S. Mahmood, B. Ikegami, K. Vigen, L. L. Henry, P. A. Schroeder, W. P. Pratt, Jr., and J. Bass, Phys. Rev. B **52**, 15426 (1995).
[10] B. Dieny, V. S. Speriosu, S. S. P. Parkin, B. A. Gurney, D. R. Wilhoit, and D. Mauri, Phys. Rev. B **43**, 1297 (1991).
[11] G. Choe and S. Gupta, Appl. Phys. Lett. **70**, 1766 (1997).
[12] L. J. van der Pauw, Philips Res. Rep. **13**, 1 (1958).
[13] S. D. Steenwyk, S. Y. Hsu, R. Loloee, J. Bass, and W. P. Pratt, Jr., J. Magn. Magn. Mater. **170**, L1 (1997); W. P. Pratt, S. D. Steenwyk, S. Y. Hsu, W.-C. Chiang, A. C. Schaefer, R. Loloee, and J. Bass, IEEE Trans. Magn. **33**, 3505 (1997).
[14] L. Piraux, S. Dubois, C. Marchal, J. M. Beuken, L. Filipozzi, J.

F. Despres, K. Ounadjela, and A. Fert, J. Magn. Magn. Mater. **156**, 317 (1996).
[15] A. C. Reilly, W. Park, R. Slater, B. Ouaglal, W. P. Pratt, Jr., and J. Bass, J. Magn. Magn. Mater. **195**, 269 (1999).
[16] C. Fierz, S.-F. Lee, W. P. Pratt, Jr., P. A. Schroeder, and J. Bass, J. Phys.: Condens. Matter **2**, 9701 (1990).
[17] A. Zambano, K. Eid, R. Loloee, W. P. Pratt, Jr., and J. Bass, J. Magn. Magn. Mater. **253**, 51 (2002).
[18] P. Holody, W. C. Chiang, R. Loloee, J. Bass, W. P. Pratt, and P. A. Schroeder, Phys. Rev. B **58**, 12230 (1998).
[19] H. Mehrer, N. Stolica, and N. A. Stolwijk, in *Diffusion in Solid Metals and Alloys*, edited by H. Mehrer, Landolt-Bornstein New Series, Group III, Vol. 26 (Springer, Berlin, 1990), p. 1.
[20] V. Vovk, G. Schmitz, and R. Kirchheim, Phys. Rev. B **69**, 104102 (2004).
[21] J. Zhang, M. A. Crimp, N. Theodoropoulou, A. Sharma, T. Haillard, R. Loloee, W. P. Pratt, Jr., and J. Bass, in *Nanoscale Magnetics and Device Applications*, MRS Symposia Proceedings No. 998E (Materials Research Society, Pittsburgh, 2007), Paper No. 0998-J09-04.
[22] T. B. Massalski, H. Okamoto, P. R. Subramanian, and L. Kacprzak, *Binary Alloy Phase Diagrams* (ASM International, Metals Park, OH, 1990), Vol. 2.
[23] C. Rath, J. E. Prieto, S. Muller, R. Miranda, and K. Heinz, Phys. Rev. B **55**, 10791 (1997).
[24] A. Fernández Guillermet, Int. J. Thermophys. **8**, 481 (1987).
[25] K. Le Dang, Appl. Phys. Lett. **63**, 108 (1993).
[26] M. J. Mills, Scr. Metall. **23**, 2061 (1989).
[27] H.-J. H. Kung, Ph.D. thesis, Cornell University, 1991.
[28] C. C. Ahn, *Transmission Electron Energy Loss Spectrometry in Materials Science and the EELS Atlas*, 2nd ed. (Wiley, New York, 2004).
[29] P. Villars, *Pearson's Handbook of Crystallographic Data for Intermetallic Phases* (ASM International, Metals Park, OH, 1991).
[30] J. Bass, in *Metals, Electronic Transport Phenomena*, edited by K.-H. Hellwege and J. L. Olsen, Landolt-Bornstein New Series, Group III, Vol. 15, Pt. a (Springer, Berlin, 1982), p. 1.
[31] D. Bozec, Ph.D. thesis, Leeds University, 2000.